Tunability of optical properties of InSb films developed by pulsed laser deposition

Tuan Nguyen Van, Etienne Laborde, Dat Tran Quang, Tung Nguyen Vu, Ca Nguyen Xuan, Do Thi Huong Giang, Thin Pham Van, Frédéric Dumas-Bouchiat, Corinne Champeaux

▶ **To cite this version:**

Tuan Nguyen Van, Etienne Laborde, Dat Tran Quang, Tung Nguyen Vu, Ca Nguyen Xuan, et al.. Tunability of optical properties of InSb films developed by pulsed laser deposition. Applied Surface Science, 2023, 619, pp.156756. ⟨10.1016/j.apsusc.2023.156756⟩. ⟨hal-04600966⟩

HAL Id: hal-04600966

https://unilim.hal.science/hal-04600966v1

Submitted on 31 Mar 2025

HAL is a multi-disciplinary open access archive for the deposit and dissemination of scientific research documents, whether they are published or not. The documents may come from teaching and research institutions in France or abroad, or from public or private research centers.

L'archive ouverte pluridisciplinaire **HAL**, est destinée au dépôt et à la diffusion de documents scientifiques de niveau recherche, publiés ou non, émanant des établissements d'enseignement et de recherche français ou étrangers, des laboratoires publics ou privés.

Distributed under a Creative Commons CC BY-NC 4.0 - Attribution - Non-commercial use - International License

Version of Record: https://www.sciencedirect.com/science/article/pii/S0169433223004324
Manuscript_1d19a4813f409900553ddd043586e3e9

Tunability of optical properties of InSb films developed by Pulsed Laser Deposition

Tuan NGUYEN VAN[1,2], Etienne LABORDE[3], Corinne CHAMPEAUX[3], Frédéric DUMAS-BOUCHIAT[3,*], Dat TRAN QUANG[1], Tung NGUYEN VU[1], Ca NGUYEN XUAN[4], Giang DO THI HUONG[2,5], Thin PHAM VAN[1,*]

[1] Department of Physics, Le Quy Don Technical University, 100000 Hanoi, Vietnam

[2] Laboratory for Micro-Nano Technology, VNU University of Engineering and Technology, Vietnam National University, Hanoi 100000, Vietnam

[3] Univ. Limoges, CNRS, IRCER, UMR 7315, 87068 Limoges, France

[4] Thai Nguyen University of Sciences, 24000 Thai Nguyen, Viet Nam

[5] Faculty of Physics Engineering and Nanotechnology, VNU University of Engineering and Technology, Vietnam National University, Hanoi 100000, Vietnam.

Corresponding author*: Frederic DUMAS-BOUCHIAT – frederic.dumas-bouchiat@unilim.fr and Thin PHAM VAN - Thinpv@lqdtu.edu.vn

Abstract

The InSb thin films were successfully prepared from binary alloy target by Pulsed Laser Deposition (PLD) onto heated Si/SiO_2 substrates at various deposition temperatures (T_d) ranging from room temperature to 400 °C. The evolutions of structural (XRD, XPS), microstructural (AFM, SEM) and optical (XPS, FTIR, RAMAN) properties as a function of deposition temperature were systematically taken into account. The analyzed results indicate that the films are well crystallized with Zinc Blende (ZB) structure for $T_d \geq$ RT. Increasing T_d induces significant signature of preferentially crystal orientations of (h11) accompanied by distinctive microstructural evolution from continuous fashion ($T_d \leq 300$ °C) to almost isolated islands feature ($T_d \geq 350$ °C). Derivations of crystallite sizes, lattice strain, dislocation density, Lotgering orientation factor, and root mean square roughness were correlated with Raman shift and XPS analysis, and optical properties. The developed thin films allow to observe the flexibility of optical band gap energy (from 0.18 eV to 0.50 eV), which is directly related to the quantum confinement effect coupled with the band-filling effect of Burstein–Moss shift.

Keywords: Pulsed laser deposition; A3B5; InSb thin film; optical bandgap; Semiconductors; optoelectronics.

I. Introduction

The high demand of optoelectronics, next-generation electronics in practical applications, has been developing extensively over the last decades [1,2], especially in remote sensing utilization, space applications [3–5], building, thermal management, and night assistance car driving. Regarding wavelengths, the optoelectronic gadgets in the infrared range this still falls far short compared to those of in visible range, which have replied on both tremendous performance and optimized cost. Infrared detection reacts to a couple of main detectors of quantum (photon) and energy. While, the first is instant but cooled cryogenically and based on narrow band-gap semiconductors such as HgCdTe, InSb or wide band-gap heterostructures (GaAs/AlGaAs or InAs/GaSb), the second is favorable to detect infrared signal of a longer responding time without cooling.

© 2023 published by Elsevier. This manuscript is made available under the CC BY NC user license
https://creativecommons.org/licenses/by-nc/4.0/

In order to assemble an infrared detector, an absorbable material in the IR regime is an important input parameter. Among the member in III-V semiconductor family, InSb has attracted intensive attention owing to (i) low toxicity (compared with wide band-gap materials); (ii) direct transition semiconductor with narrow band-gap of 0.17 eV (at room temperature) which is fundamental parameter relating to usability of materials in optical, electronic, and energy applications [6]; (iii) the highest hole/electron mobility of 7.7 $m^2.V^{-1}.s^{-1}$; (iv) more simpler combination of binary alloy; or (v) even with quantum electron transport owing to homogeneous growth at large scale and better covalent bonding accompanied by a reasonable cost compared with HgCdTe material. Moreover, InSb pushes the optical absorption above 3 µm-a fascinating threshold. Firstly, this value corresponds to the value above whose thermal emission of warmer conventional sources from reflection such as the sun. Secondly, conducting thermal imaging, the transparency window is necessary and there are two types of windows of mid-wave infrared from 3 µm - 5 µm in the atmosphere spans and long-wave infrared from 8 µm - 12 µm.

To date, InSb thin films with good optical properties have been deposited by sputtering [7,8], molecular beam epitaxy (MBE) [9] or thermal vaporization [10]. However, growth by MBE requires single crystal substrates and demanding conditions during/prior to deposition, i.e, CdTe with equivalent lattice parameters which cause high cost production and complex fabrication process. The InSb crystallization was induced by preparing films onto heated substrates both with post-annealing and without post-annealing methods [7,11–13]. To our best knowledge, there has been only single article have been done so far which truly dedicates the InSb thin film by Pulsed Laser Deposition (PLD) on CdTe [14] by investigating the transmission and crystallization properties of thin films with respect to composition with/off stoichiometry. PLD is a type of physical vapour deposition, and has been known for years to be one of the most elegant and straightforward techniques in fabrication complex materials owing to the stoichiometric transfer from the ablated target to the opposite substrate for thin film growth [15]. PLD is of a wide range of controllable *in-situ* deposition parameters such as laser fluence, laser wavelength, target-substrate distance, deposition ambient pressure (P_a), deposition temperature (T_d), etc. It is fascinating to note that the physical properties of deposited films are massively induced by adjusting the fabricating parameters during the deposition [15–18]. T_d variable is among the most crucial processing parameters for thin film properties, which considerably influence the plasma plume formation, and lifetime of adatoms. In order to enrich the fabrication methods and comprehend in details about deposited InSb thin films, in this letter, the influence of InSb thin films grown by PLD onto inexpensive Si/SiO_2 substrate with various T_d on the crystallization, microstructure and optical properties will be investigated and correlated systematically.

II. Experimental description

Single layered InSb thin films were deposited on silicon substrate (100) with thermally oxidized layer up to 100 nm using PLD with base pressure of 1×10^{-7} mbar and depositing pressure of 5×10^{-7} mbar in vacuum. Note that the reduction in pressure while depositing in vacuum is due to thermal desorption from the heater. The initial compound alloy InSb target (in polycrystallized state) was provided by Neyco Inc, France with high purity of 99.999%. The target with molar ratio of In:Sb = 50:50; diameter 2.54 cm; thickness 4 mm; was mechanically attached to the target holder with a certain rotation speed. The use of rotation is to limit the droplet formation on the deposited film owing to the target roughening and target aging [19,20]. The excimer laser beam first passes through an aperture to select the best homogeneous area and later direct to the InSb target with a defined frequency of 10 Hz. The characteristics of the typical PLD system used in this study are employed from an excimer laser (KrF Light Machinery IPEX 742, λ = 248 nm, pulse duration 25 ns), with the laser fluence remaining at a

constant of 2 J.cm^{-2}. During the deposition, the Si/SiO_2 substrate was heated by a backside-heating halogen lamp through heat radiation from room temperature (25 °C, RT) to 400 °C, and the distance between target and substrate was kept at 40 mm.

Prior to deposition, the target was pre-ablated to clean its surface by around 10000 laser pulses; the Si/SiO_2 substrate with 1 cm ×1 cm and thickness of 500 µm was subjected to conventional cleansing sequences of embedding in acetone, ethanol, and deionized water during 5 minutes each, in an ultrasonic bath; the substrate was finally dried by pressurized Ar gas, and ready to place in the deposition chamber. Sets of deposited InSb thin films were then characterized by using X-Ray diffractometer for structural properties in a Bragg-Brentano geometry of θ-2θ configuration (KFL Cu Tube, Cu-$K_{\alpha 1}$ radiation) with step size of 0.008°, acquisition time of 3 seconds per step, and a rotation of the sample at 30 rpm. While Atomic Force Microscopy (AFM) associates with Scanning Microscopy (SEM) allow to quantify the morphology, the X-ray Photoelectron Spectroscopy (XPS) and Energy Dispersive X-ray Spectroscopy (EDS) favor to determine the compositional elements and chemical states of deposited films. The optical properties are later validated by using Fourier Transform InfraRed spectroscopy (FTIR) and Raman spectroscopy (RAMAN). Characterizations were all performed at RT.

III. Results and Discussion

The particularity of congruent process in PLD, for a set of InSb thin films, with nominal thickness of 500 nm by keeping 20000 pulses of laser deposition, deposited at a wide range of deposition temperatures - T_d and a constant deposition vacuum pressure of 5×10^{-7} mbar, were tested experimentally by performing EDS measurements. Starting from equiatomic alloy target, the dependence of average In/Sb atomic ratio of the deposited films as a function of T_d is depicted in Figure 1. Obviously, the In/Sb ratio of atoms in the films grows slightly with increasing T_d from around 0.8 at RT to stagnant values close to unity at 300 °C - 400 °C. At low T_d (< 300 °C), the ratio is significant lower than that of equiatomic ratio of unity (blue dashed line) obtained from either the target itself or films deposited at higher T_d (300 °C - 400 °C). It could be said that, in this circumstance at low T_d, the obtained ratio values somewhat fall short of the stoichiometric transfer value of unity in PLD. The steep decline in the In/Sb atomic ratio at low T_d might be attributed to: (i) differences in melting point of the compositional elements, i. e., In (~156 °C) and Sb (four folds larger, ~631°C); (ii) variation in atomic masses, i. e., In (114.82 u) and Sb (121.76 u); and (iii) evaporation/re-sputtering effect during deposition process that leads to the redistribution of composition in target surface [15,21]. However at higher T_d, the In/Sb atomically compositional ratios vary around the unity, which may be ascribed to the comparable values of T_d and melting point of InSb alloy (~527 °C) allowing elemental species/molecules to find proper minimal energy locations on substrate during the thin film growth, without rebounding back to the plasma plume/the target surface [15]. Additional comprehensive reports on varying elemental composition of deposited films with T_d might be assigned to variation of species with various vapor pressures, modifying the plasma plume expansion, deposition rate, and mobility of adatoms on the heated substrate [15,22–24]. It is noted that the plasma plume in the PLD process can contain single-elemental atoms, alloy molecules, and other compounds (resulting from reactions of compositional elements with other materials such as residual oxygen).

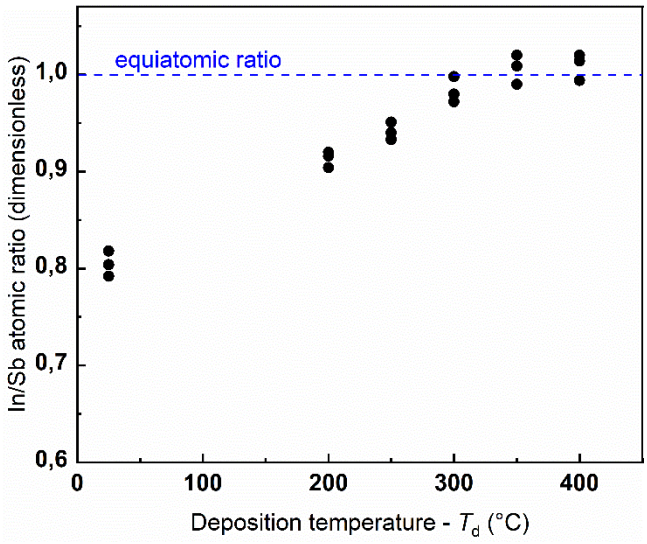

Figure 1: The dependence of In/Sb atomic ratio of deposited InSb thin films on various T_d, in vacuum with P_a = 5×10^{-7} mbar, performed by EDS measurements equiped in SEM. The blue dashed line corresponds to the equiatomic ratio of unity.

The scanning θ - 2θ XRD patterns performed on Bruker D8 Advance Series II (equipped with a focusing $K_{\alpha1}$ primary Germanium monochromator, detector LynxEye model "A17-B60", primary 2.5° Soller slits, 1mm fixed divergence slits, secondary 2.5° Soller slits) of the deposited InSb films ranging from RT to 400 °C are shown in Figure 2. In all diffractograms, the signature from the substrate of Si is visible with forbidden peak and (400) reflection at ~32.9° and ~69.3°, respectively. RT deposited film shows no diffraction peaks of InSb and Sb reflecting the film in amorphous state or crystallized in short range order. Orientations of (111), (220), and (311) from the concerned phase - InSb, taken from ICSD reference card - PDF: 04-001-0014, with Zinc Blende (ZB) face-centered cubic (*fcc*) structure of space group F - 43m (216) are indexed in all films deposited above RT, while reflections corresponding to (400) and (511) indices disappear at T_d = RT, 200 °C, and 400 °C, and peak of Sb (012) enrich phase is identified for film deposited at low $T_d \leq 250$ °C only. Note that the peak shifts are identified for the films deposited at low $T_d \leq 250$ °C, as demonstrated for (220) reflection in the enlarged portion of the XRD patterns (Figure 2). This shift becomes higher and higher when the In/Sb ratio drops well below the equiatomic one. Observation of Sb surplus sign and peak shift at low T_d agree well with analysed EDS results above and the phase diagram of InSb material of coexistence with both InSb and Sb forms (as films are off equiatomic composition) [25]. Relative intensities between (111) and (220) orientations extracted from the diffractogram illustrate that these relative intensities climb from 0.03 (T_d = 200 °C) to 0.11 (T_d = 250 °C) and sluggish value of around 4.2 (high T_d = 300 °C - 400 °C). Increasing of relative intensity of (111) orientation compared with other orientations, such as (220), show that (i) the dominance of the InSb phase exists in the lowest energy state; and (ii) improvement in crystallinity of the phase, as T_d rises up.

From the XRD patterns, the lattice parameter of the deposited films with *fcc* structure has been estimated by employing the following relationships (Equation 1):

$$d_{hkl} = \frac{\lambda}{2\sin\theta} \quad \text{and} \quad a = d_{hkl}\sqrt{h^2 + k^2 + l^2} \qquad \text{Equation 1}$$

where d_{hkl} is the distance of crystallographic plane; h, k, and l are Miller crystallographic indices, λ = 0.15406 nm is the emitted X-ray wavelength of the diffractometer, θ is the Bragg angle corresponding to indicated Miller indices. The average lattice constant a estimated for (111), (220), (311), (331), and

(511) orientations is about 0.6474 nm ± 0.007 nm compared to that of 0.6479 nm taken from the reference card of InSb material grown by floating melting zone technique. The two above values are comparable to 0.6479 nm obtained for bulk material in literature [26,27], which indicates that InSb material deposited in thin film form in this work is of good crystal quality as the bulk form.

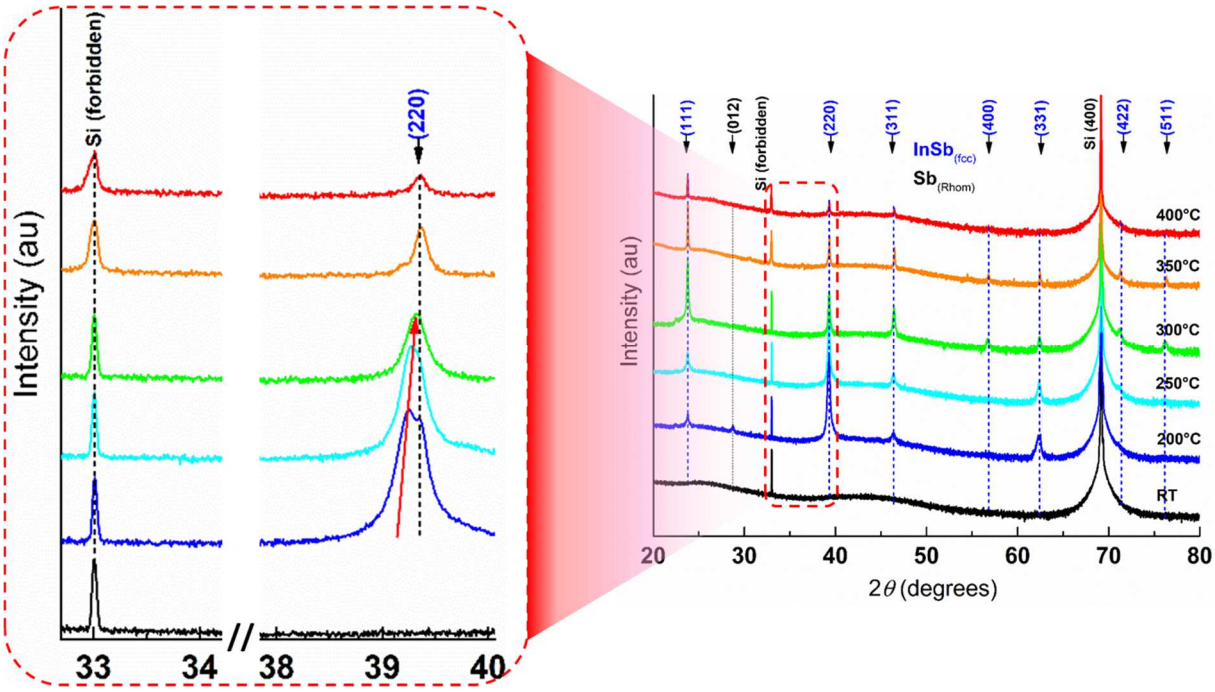

Figure 2: XRD patterns with scan from 20° to 80° and the enlarged part, of InSb thin films deposited on Si/SiO_2 (100 nm) substrate at various T_d in the range from RT to 400 °C, in vacuum with $P_a = 5\times10^{-7}$ mbar.

Additional information from XRD patterns can be extracted and correlated further such as average crystallite size (D_{ave}, nm), lattice strain (ε, %), and dislocation density (σ, cm^{-2}). These quantities require values of the Full Width at Half Maximum (β), which is directly influenced by peak broadening of the sample due to the nanocrystal effect. However, regular XRD measurement normally comes up with the diffracted peak broadening induced by a variety of sources including (i) the sample itself, which may consist of many involved defects of the crystal, i. e., crystallite size, microstrain, solid inhomogeneity, and temperature factors; and (ii) the instrument, i. e., X-Ray source (wavelength widths, superposition of K_α doublet) and X-Ray machine optics (X-ray focus, dispersion, absorption, divergence, misalignments, detector slits) [28,29]. In this study, in order to achieve the actual broadening due to the sample, the instrumental contribution to the line broadening was eliminated by using a standard reference material LaB_6 (SRM660). The corrected broadening can be corrected by applying the following formula [28,30]:

$$\beta_c^2 = \beta_m^2 - \beta_i^2 \qquad \text{Equation 2}$$

where β_m, β_i, and β_c are the measured, instrumental, and corrected broadenings, respectively. Note that calculation of β_c for InSb sample can be performed in three main steps: (i) each XRD peak from both LaB_6 sample and InSb thin films was simulated by a pseudo-Voigt function, and the integral breadth or β was calculated; (ii) for LaB_6 sample, plotting β_i with respect to the Bragg diffraction angle (2θ) associated with performing a regression of the plot to obtain the function of $\beta_i(2\theta)$; and (iii) for each diffracted angle of InSb thin film, calculating the β_i of the instrument thanks to the step (ii), then β_c was obtained given by Equation 2. The corrected broadening β_c associated with the use of Williamson-Hall analysis provide the D_{ave} and ε values (Equation 3) [28,30,31], and the σ value (Equation 4) [32], as follows:

$$\beta_c \cos\theta = \frac{0.9\lambda}{D_{ave}} + 4\varepsilon \sin\theta \qquad \text{Equation 3}$$

$$\sigma = \frac{3n}{D_{ave}^2} \qquad \text{Equation 4}$$

By graphing the $\beta_c\cos\theta$ as a function of $\sin\theta$, known as the Williamson-Hall plot, the D_{ave} and ε values relating to intercepts and slopes can be estimated, respectively. Note that σ can follow from various classic formulae, i. e., (i) if threading dislocations are randomly distributed, then $\sigma = \frac{\beta_{ro\_c}^2}{2\pi b^2 \ln 2}; \left|\vec{b}\right| = \frac{a}{2}\sqrt{h^2+k^2+l^2}$ is applied (β_{ro_c} is the Full Width at Half Maximum of the rocking curve of the reflections corresponding to the Burger's vector $\vec{b}$) [33–35]; and (ii) if grain boundaries are formed and the dislocations lying between the boundaries, then minimum σ is given by Equation 4 with n =1, which is applied for annealed metals and/or highly deformed metals. For simplicity, this work uses Equation 4 (n = 1) to roughly approximate the σ.

Figure 3a presents the Williamson-Hall plot for the investigated InSb film (the corresponding Miller indices are also included). The calculated average crystallite size - D_{ave} and lattice strain - ε as a function of T_d, are illustrated in Figure 3b. The D_{ave} increases with increasing T_d, i, e., from around 138 nm at T_d = 200 °C to 2.5 folds of about 345 nm at T_d = 400 °C, which might be attributed to the enhancement of crystallinity at higher T_d by agglomerating several crystallites, indicated previously. In contrast with tendency to D_{ave} with T_d, the ε tends to decrease from 0.004 at T_d = 200 °C at to 0.002 at T_d = 400 °C. The growth of crystallite size is correlated with a reduction in the ε, which is due to the displacement of the atoms from their atomic positions in the crystal structure [36] and possibly reflecting through the crystallinity improvement.

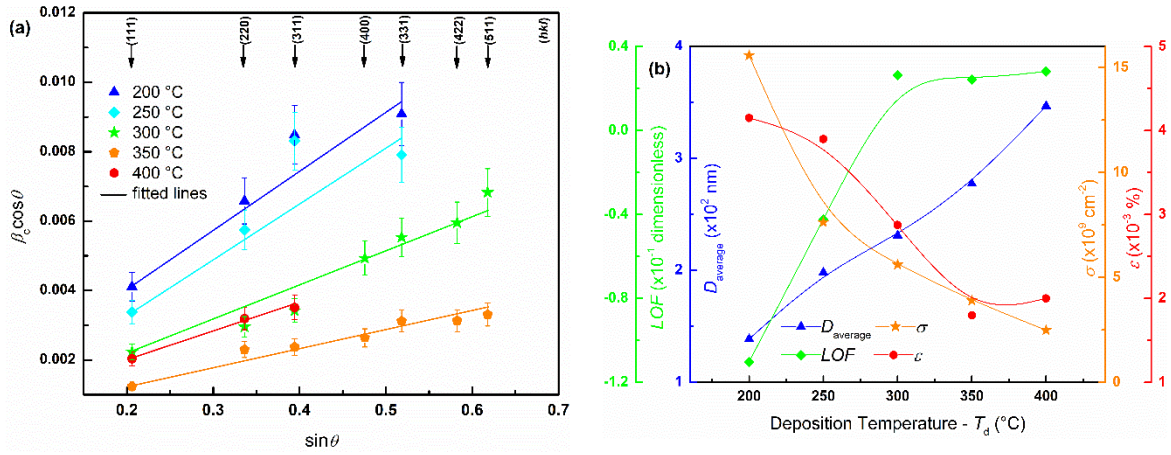

Figure 3: (a) The Williamson-Hall plot for the set of InSb films deposited on Si/SiO_2 (100 nm) substrate at various T_d in the range from 200 °C to 400 °C, in vacuum with $P_a = 5\times10^{-7}$ mbar; and (b) The derived parameters D_{ave}, ε, σ, and *LOF* as a function of T_d for this set of film. The colored solid lines in (b) are guides to the eyes.

As also depicted in Figure 3b, the σ value decreases from 15.5×10^9 cm^{-2} to 2.5×10^9 cm^{-2} with the development of T_d. These observed values are in good agreement with the σ in GaN epitaxial layer, which represents for most semiconductor thin films [37,38]. The reduction of σ is generally related to the improvement of crystalline quality, which is indirectly reflected from the experimental β_c parameter. The prevailing assumption for the reduction of σ is assigned to the annealing under presence of a driving force, which can be either thermal fluctuation or mechanical stress resulting in dislocation annihilation (a pair of dislocation with opposite sign attract and annihilate pairwise), and diffusion of dislocations at the surface. Namely, such dislocations and/or adatoms become significantly mobile with specific

crystallographic glide facets at temperature above the brittle-ductile transition temperature of around 150 °C for InSb [39,40]. While the mobility of dislocations is usually induced by vacancy diffusion allowing dislocations to move out of the glide plane well above the transition temperature, the driving force promotes the dislocations defeating the activation energy threshold to become mobile. It is therefore, higher T_d, lower activation energy results in more mobility and reduction in dislocation density.

The relative intensities of diffracted orientations also reveal the preferential growth state of developed films, in this circumstance, the Lotgering orientation factor (*LOF*) is frequently used to define the texture characteristic of the films, and expressed as follows [41]:

$$p = \frac{\sum (abc)_{sample}}{\sum_{all} (hkl)_{sample}}; p_o = \frac{\sum (abc)_{powder}}{\sum_{all} (hkl)_{powder}}; \text{and } LOF = \frac{p - p_o}{1 - p_o} \qquad \text{Equation 5}$$

where p is the ratio between the sum of intensities of the interested (abc) reflections and to the sum of all reflections, p_o is the value for the bulk/powder form. In this circumstance, the *LOF* varies from a certain negative value to unity, for which negative denotes for other preferential orientation rather than (*abc*), 0 stands for random orientation, and the unity is for fully preferential orientation. Variation of *LOF* value of (*h*11) family planes (h = 1, 3, 5), estimated from XRD patterns, is illustrated in Figure 3b. At low deposition T_d ($T_d \leq 250$ °C), *LOF* values are all negative showing other reflections dominating the crystallized films rather than (*h*11), i. e., (200) reflection. The *LOF* values become positive, and reach to values of around 0.3 for films deposited at higher T_d ($T_d \geq 300$ °C) depicting signature of partly textured films with lowest energy planes of (*h*11) reflections.

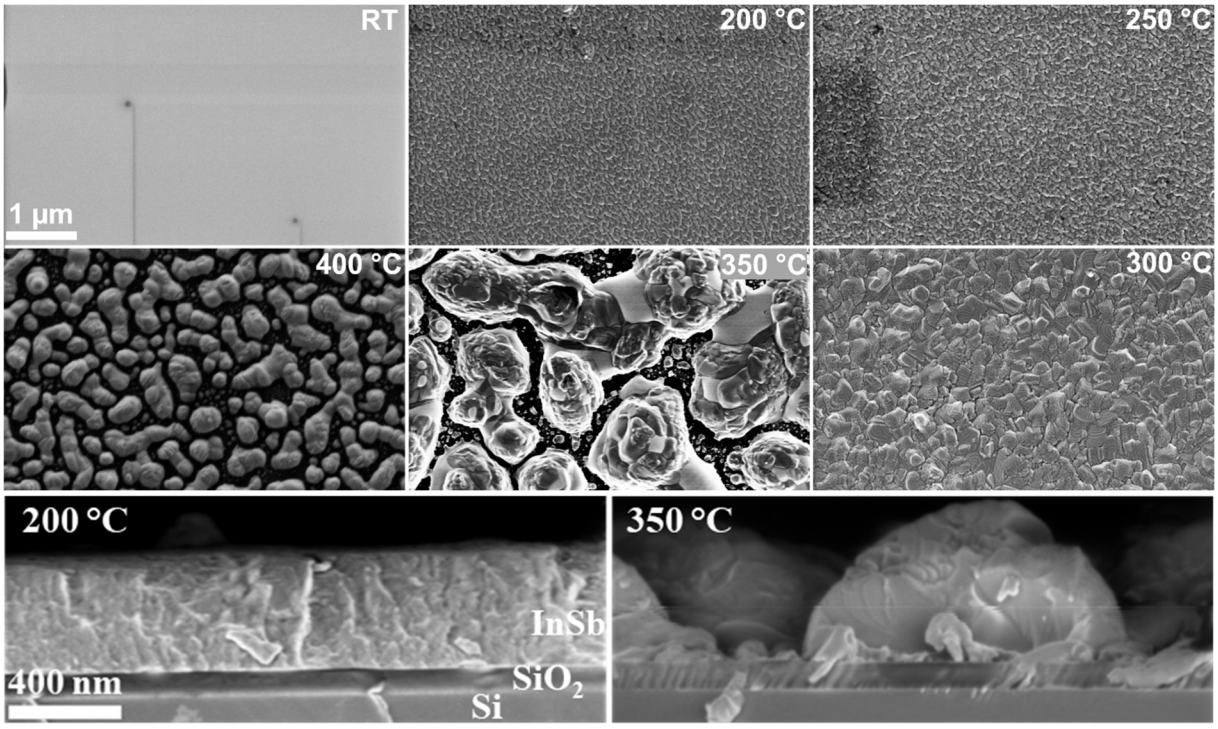

Figure 4: (top) The plane-view SEM images for the set of InSb films deposited on Si/SiO_2 (100 nm) substrate at various T_d in the range from RT to 400 °C, in vacuum with $P_a = 5\times10^{-7}$ mbar; and (down) the typical cross-sectional SEM images showing structure of the films deposited at 200 °C and 350 °C.

The evolution of surface morphology of InSb films, performed on plane-view with SEM In-lens mode, as a function of T_d is demonstrated in Figure 4 (top). The microstructure of the deposited films is clearly distinguishable. While films deposited at lower T_d ($T_d \leq 300$ °C) are covered by closely packed

islands with average size increasing from a few tens nm up to 400 nm, higher T_d (350 °C $\leq T_d \leq$ 400 °C) lead to completely isolated island feature with diameter approaching more than 5 µm on an underlying tier of smaller grains with diameter < 200 nm. Grains of sample deposited at 350 °C are relatively larger than that of sample developed at 400 °C, constituted of clusters of twisted smaller platelet-like grains with diameter less than 1 µm. Obviously, the observable grains, in this circumstance, contain multiple crystallites. The distinct characteristic of microstructure for samples deposited at 350 °C and 400 °C, closing to the melting point of InSb alloy ~527 °C, could be attributed to the Ostwald Ripening mechanism [42] and dewetting effect [43], by which the compositional elements and/or compound on the film surface are more energetically unstable compared to those within. Such unstable species frequently enter a solution that collapses the particle overtime and introduce additional free molecules in the solution. Once the particles reach the supersaturated state of shrinking particles, the free molecules will settle in the larger particles, leading to reduction in size of smaller particles and growth even larger of larger particles.

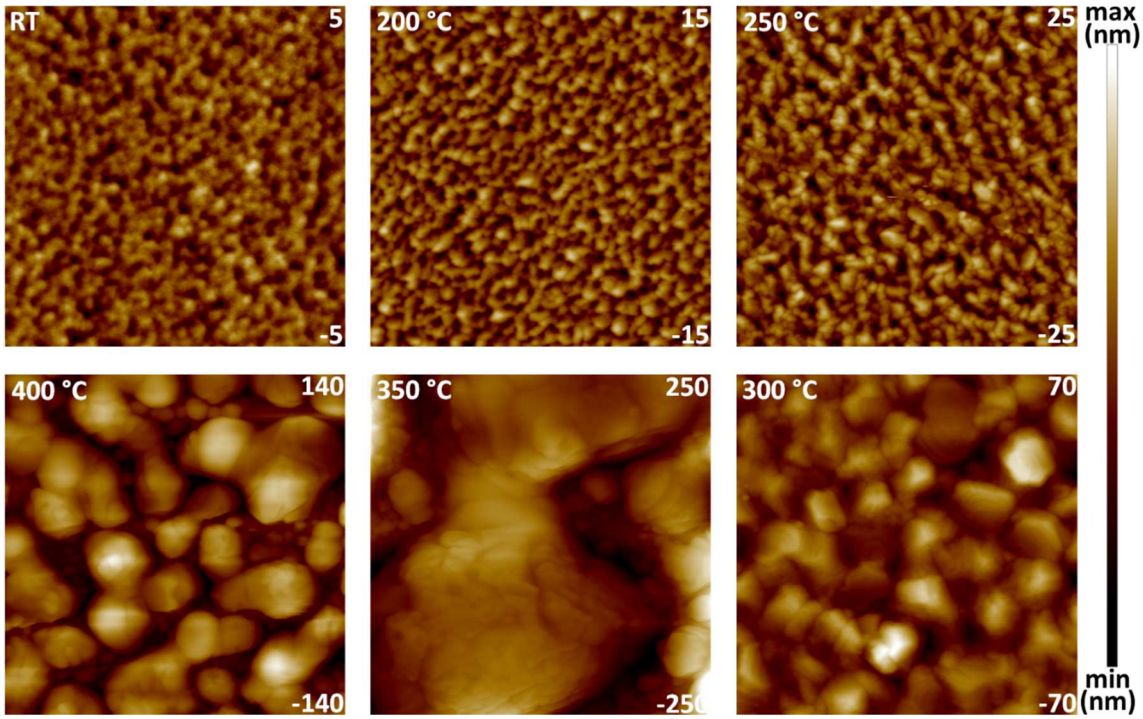

Figure 5: The evolution of AFM surface morphology of InSb films deposited on Si/SiO_2 (100 nm) substrate at various T_d in the range from RT to 400 °C, in vacuum with $P_a = 5\times10^{-7}$ mbar. Size of each single image is 2 µm × 2 µm. The z height variations from minimum to maximum values, of the performed films are dedicated at the right of the corresponding image.

Two typical cross-sectional SEM images displaying structure of the films deposited at 200 °C and 350 °C, are presented in Figure 4 (down), which illustrates three layers including the substrate of the deposited films as Si/SiO_2 (~ 100 nm)/InSb (~ 500 nm). Thickness obtained from SEM images are around the nominal thickness of 500 nm. The variation in deposited thickness compared to the normal one could be attributed to the distinct microstructures, re-sputtering effect, and reduction in laser fluence owing to the attached materials on the entrance PLD window over time of deposition. The cross-sectional morphologies concede willingly the plan-view microstructures, depicted in Figure 4 (top), i. e., continuous pattern composed of very fine grains at T_d = 200 °C, and become completely isolated islands at T_d = 350 °C. The isolated island growth at high T_d inspires more porosity, voids, and hence it is consistent with reduction of mobility of adatoms determined in Figure 3b.

AFM analysis, indicated in Figure 5, was characterized on top of films with scanning area of 2 µm × 2 µm. The overall morphologies of these images are coherent with the microstructure observed by SEM. The extracted information from AFM specifies that the root mean square (rms) surface roughness escalates from ~0.5 nm, for film deposited at RT, to a maximum value of ~38 nm for film fabricated at 350 °C, and later gently decreases to ~37 nm at higher T_d of 400 °C (shown in Figure 6). The high values of rms roughness for film deposited at 350 °C and above well agree with the isolated islands, resulting in high variation in the z height for the same area of interest, which are evidenced in Figure 4 and Figure 5. The increase of rms roughness with increasing substrate temperature might be owing to the improvement of crystallization at higher T_d, reflected by increasing D_{ave} and *LOF* parameters, which were already expressed previously.

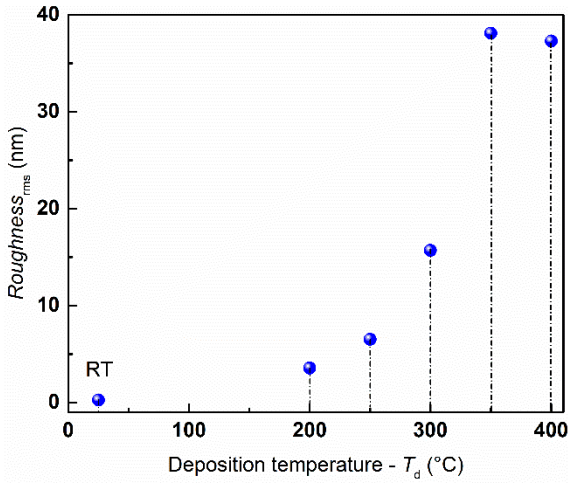

Figure 6: The variation of rms roughness as a function of depostion temperature, extracted from AFM images presented in Figure 5.

The vibrations of molecules and/or atoms inside the materials, under excitation of a laser source, which result in the relative distance between the molecules varied, and thus the Raman spectroscopy is obtained. The Raman shift, presented in Figure 7, was characterized at RT, under a laser source with wavelength of 785 nm. The characteristic Raman spectrum for InSb material with well crystallized material is mainly governed by two phonon modes of vibrations of transverse optical – TO (~180 cm^{-1}) and longitudinal optical – LO (~191 cm^{-1}), induced by the first order of Raman scattering corresponding to energy band gaps of 1.9 eV and 2.4 eV, which are splitted by spin-orbit coupling from a direct energy bandgap of 1.8 eV [44,45]. All deposited films have these two modes, though they are not readily visible for film deposited at RT. These two pronounced peaks shifted to lower wavenumber values compared to bulk form corresponding to ~220 cm^{-1} (TO) and ~240 cm^{-1} (LO), and as other polar semiconductors crystallized with ZB atomic structure, i. e., GaAs, by which the LO value is higher than that of the TO [46]. Increasing T_d drives the growth in relative intensities of TO, and LO modes, approaching maximum in sample deposited at 350 °C, and then slightly reducing when T_d increases further. These observations are agreed with increasing textured properties of the films (expressed by structural and microstructural analyses) followed by *LOF*, and rms roughness parameters. This means that films deposited at low $T_d \leq$ 250 °C come up with amorphous phase (RT), or crystallized in a very short range order (RT), or partly crystallized (200 °C, 250 °C), and the primary part of crystallized phase dominates the films deposited at higher T_d. Additional peaks appearing at ~146 cm^{-1}, in films deposited at $T_d \leq$ 200 °C, are attributed to high density of ruptured Sb-Sb bonds, regularly found in amorphous material [47]. The Raman micrographs with Sb-Sb bonds demonstrate a good agreement of minor crystallized phase and Sb in excess in the films, indicated by EDS and XRD.

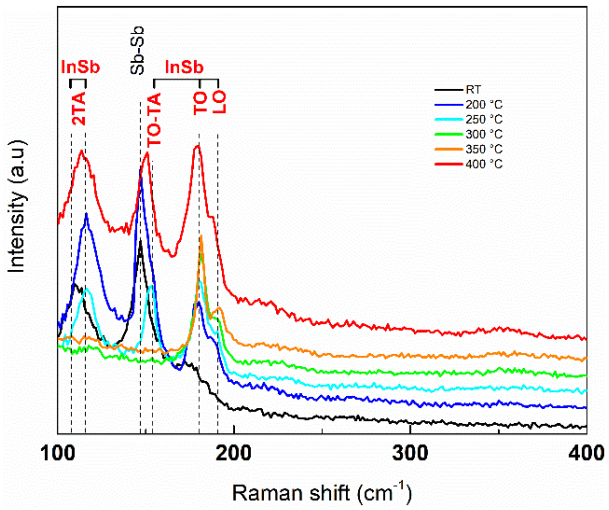

Figure 7: The Raman shift of InSb films, deposited on Si/SiO_2 (100 nm) substrate at various T_d in the range from RT to 400 °C, in vacuum with $P_a = 5\times10^{-7}$ mbar, was excited by a laser source of 785 nm and measured at RT.

Two more peaks, accompanied by low intense peaks of TO and LO, identified at 153 cm^{-1}, and 109 cm^{-1} for films deposited at (RT, 200 °C, 250 °C, and 400 °C), are ascribed to TO-TA and 2TA phonon modes, respectively, which could be correlated to the second order of Raman scattering [45]. These peaks are signatures of non-optimized films in terms of elemental composition (non-stoichiometric) and/or crystallographic structure (not textured or amorphous state) [48,49]. In comparison between these films, a Raman shift ~7 cm^{-1} from the dominant peak at 109 cm^{-1} (film deposited at RT), might not due to the phonon confinement only but could further assigned to augmentation of crystallized phase, as evidenced in XRD, inspiring different degrees of internal stress/strain of deposited films [50]. In case of phonon confinement only, the Raman shift should take place at lower wavenumber owing to the zero-wave vector selection rule close to Brillouin zone and negative slopes of the phonon dispersion curves at the zone center [46]. Moreover, the appearance of these two peaks might relate to the presence of X-ray reflections of (400) and (511) as identified in Figure 2. Note that the Raman shift of InSb films from 400 cm^{-1} to ~1300 cm^{-1} are straight lines, and hence they are not included in Figure 7. The characterization of Raman spectroscopy also suggests that deposition at low $T_d \leq 250$ °C or too high $T_d = 400$ °C, produces films with Sb in surplus and minor crystallized InSb phase, while elevated T_d (300 °C - 350 °C) promotes more textured films with near equi-atomic composition and major part of crystallized InSb phase.

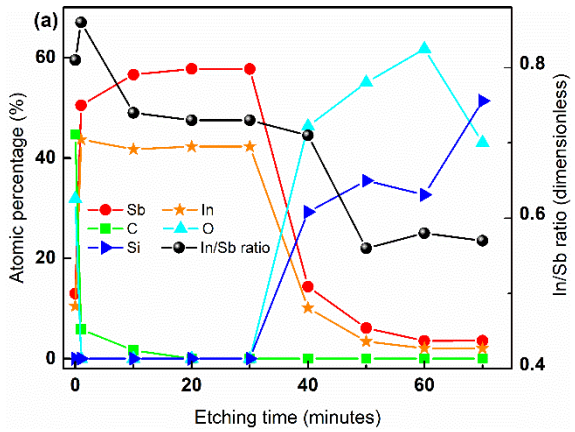

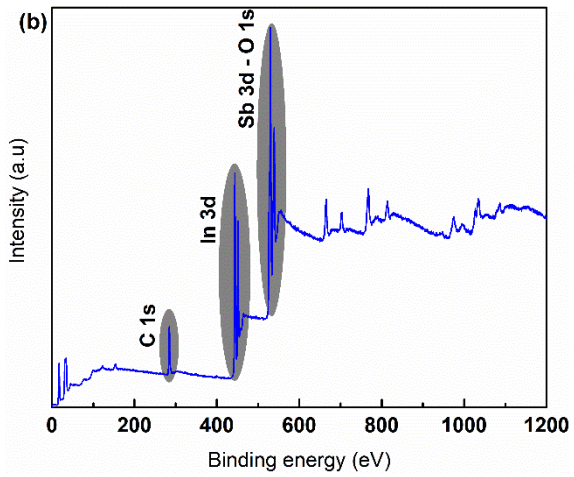

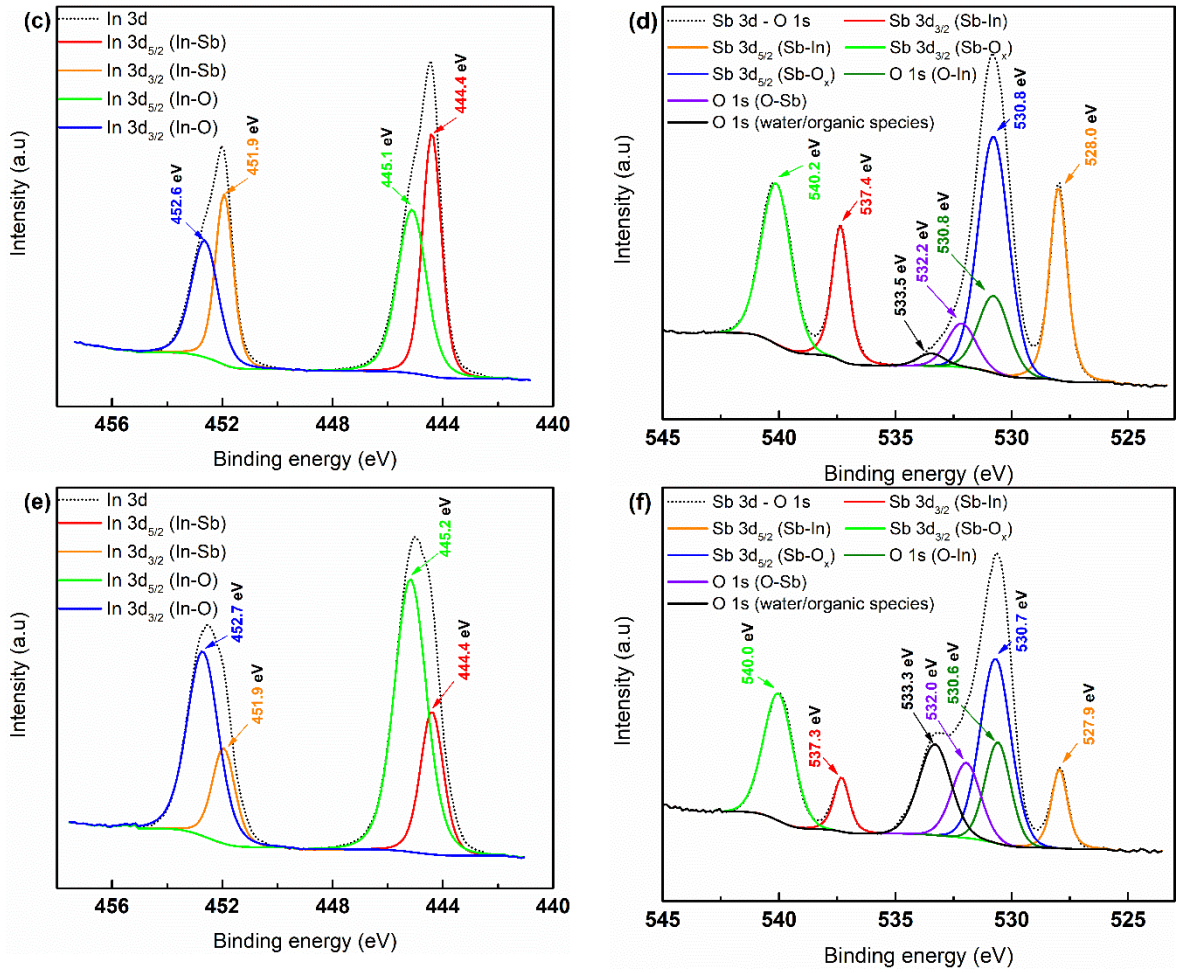

Figure 8: The XPS characterization of typical InSb thin films. (a) the atomic percentage of the compositional elements and In/Sb ratio in the film deposited at RT as a function of etching time through the film thickness; (b) the survey spectra in the whole range of binding energy (BE) for film deposited at RT; Region of the high resolution photoelectron spectra of InSb films with In 3d cores and Sb 3d – O 1s cores for films deposited at RT (c) and (d); for film deposited at 400 °C (e) and (f), respectively.

In order to access more about the chemical state and the overall electronic structure of the deposited films, two surface states of typical thin films deposited at RT and 400 °C were characterized with XPS (Figure 8). In the measurement, the ion beam was accelerated to etch the films, perpendicular to the film surface, under vacuum of Ar ambient gas at 5 keV and 7 mA, resulting in a raster size of ~3 mm × 3 mm. The XPS spectra were measured using an X-Ray Photoemission Spectrometer (KRATOS, Axis Ultra DLD) at a residual pressure in the analyser chamber at around 5×10^{-9} Torr ($\sim6\times10^{-9}$ mbar), using a monochromatic Al K_α source (1486.6 eV). The electron energy analyser is normal to the surface and the pass energy for High Resolution spectra is 20 eV, and 160 eV for survey spectra. The energy scale of the spectrometer was calibrated using the binding energy of the Au $4f_{7/2}$ peak at 84.0 eV and the Cu $2p_{3/2}$ peak at 362.2 eV as references. Core level spectra were fitted with GL (Gaussian/Lorentzian product) and SGL (Gaussian/Lorentzian sum) functions after Shirley background subtraction, using CasaXPS Software. To compensate charging effect, all spectra were referenced to the In $3d_{5/2}$ (in InSb) at 444.4 eV.

Figure 8a presents the elemental composition distribution with respect to etching time (or the film thickness). The film layers were revealed as InSb/SiO_2/Si. As etching inside the film layer, the C sign from surrounding media is dramatically reduced, while the O and Si signatures from the substrate

maintain at low level. In and Sb signs are all visible from the beginning. After about 30 minutes of etching, it reaches the interlayer between the InSb and SiO_2, leading to increased signatures of (O and Si) and reducing contents of (In and Sb). The In/Sb ratio at the surface is equivalent with values obtained from EDS investigation. However, penetration through the film thickness results in slightly smaller In/Sb ratios (~ 0.73) compared to those closed to the surface (~0.81). This can be attributed to the etching procedure modifying composition inside and outside of the raster area. The overall survey spectrum of the surface for this film is demonstrated in Figure 8b. The concerned elements in this work are In, and Sb and thus high resolution XPS spectra for these elements were performed. Figure 8c to Figure 8f provide the In 3d and Sb 3d asscociated with O 1s core levels with high resolution photoelectron spectra , performed on the film surfaces, for films deposited at RT (Figure 8c and Figure 8d), and 400 °C (Figure 8e and Figure 8f).

Figure 8c exhibits the In–Sb bonds identified at binding energies (BE) of In_3d doublet components of 444.4 eV and 451.9 eV corresponding to the In_3d peaks splitted into $3d_{5/2}$ and $3d_{3/2}$ owing to spin-orbit interaction. These results: (i) are consistent with the BE of In_3d for InSb bulk form at 444.2 and 451.8 eV [51], and (ii) might relate to the Raman observations indicated in previous analysis. Film deposition at RT was observed a light shift (0.2 eV) towards higher energies, which is equivalent with the value obtained in films fabricated by electrodeposition techniques [52]. The electronics states of In-O bonds are also indexed at BE of 445.1 eV and 452.6 eV. Doing statistics for areas under the curves of In-Sb and In-O bondings, the area intensity percentage of In-Sb is about 49% compared to ~51% for In-O bonds. Regarding the Sb_3d – O_1s spectra (Figure 8d), the Sb_3d and O_1s peaks are overlaid. A very keen decomposition was made to distinguish the contribution of each single element, i. e., two couples of doublet of Sb_3d (Sb-In and Sb-O_x bonds) and a triplet of O_1s (O-In, O-Sb, and O- from water or organic species). While doublet components for Sb-In bonds are found at 528.0 eV and 537.4 eV, the components for Sb-O_x bonds are at BE of 530.8 eV and 540.2 eV, respectively, similar to values obtained from other studies [51,53]. Note that the Sb-O_x represents for Sb_2O_3 and/or Sb_2O_5. Three components of O_1s are at 530.8 eV (O-In), 532.2 eV (O-Sb), and 533.5 eV (O-from water or organic species). Area intensity percentages for Sb-In, Sb-O_x, and O_1s bonds are ~28%, ~54%, and ~18%, respectively.

Increasing T_d to 400 °C leads to a slightly BE shift of In-O, Sb-In, Sb-O_x, and even O_1s (Figure 8e, and f), with values ranging from 0.1 eV to 0.2 eV, compared to film deposited at RT. In addition, the area intensity percentage of In-Sb bonds decreases significantly from 49% to ~27% (Figure 8e), in contrast to area intensity percentage In-O bonds, which shows ~22% increase (Figure 8e) from 51% in film deposited at RT. These XPS analyses indicate that (i) the peaks in In_3d are shifted towards higher BE and Sb_3d peaks shifted towards the lower ones demonstrating a positive charge transfer from Sb to In on forming InSb [51]; (ii) films are partly oxidized owing to variety of sources, i. e., resident oxygen inside the PLD chamber, high temperature activate the oxidation process, exposure films in amostpheric air during other characterizations, i. e., XRD, SEM, RAMAN, etc, though they are not observed by means of XRD. Note that the penetration depth of XPS is normally less than 10 nm from the analysis surface.

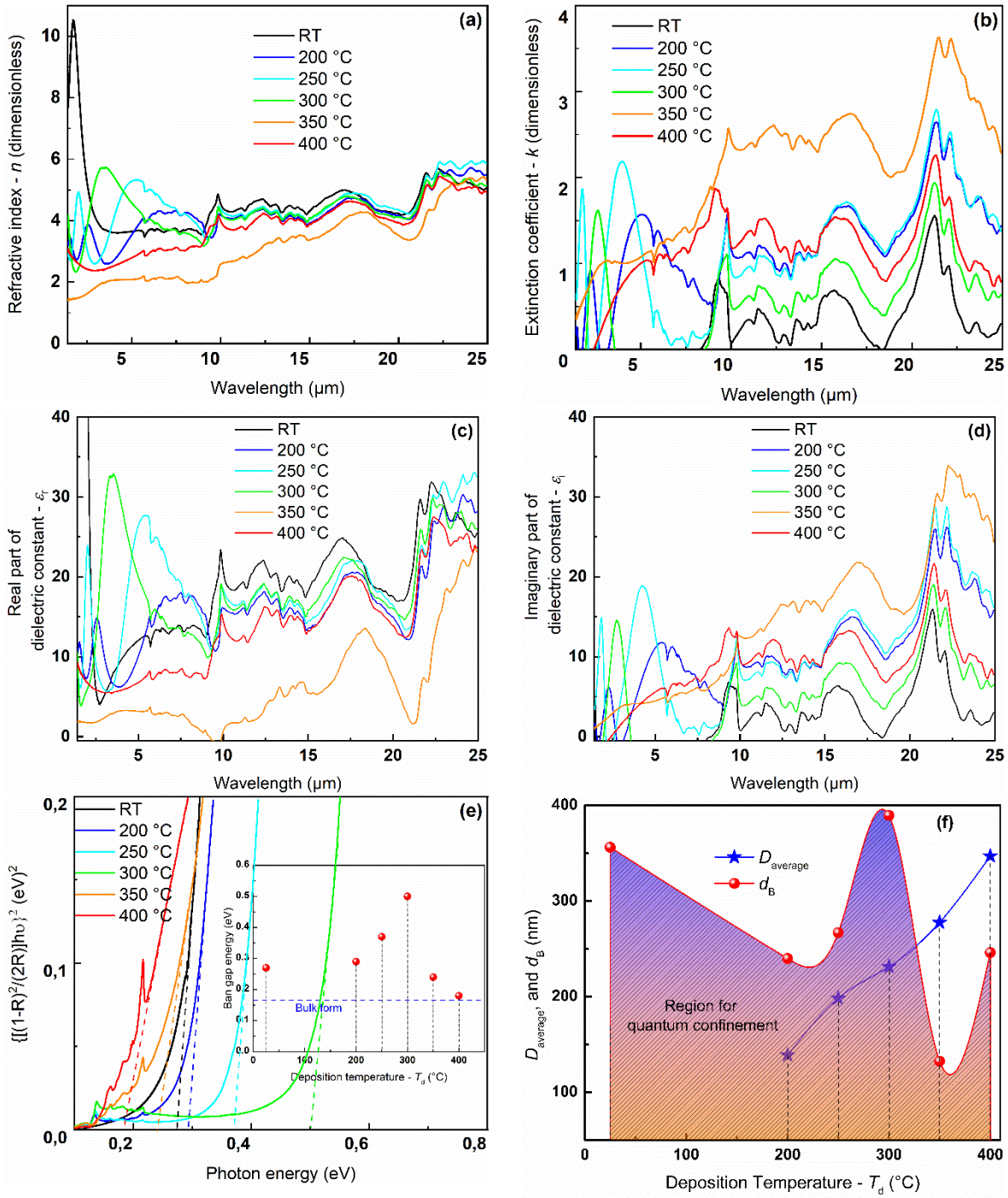

Figure 9: Optical properties of the InSb thin films characterized by FTIR at RT. (a) The refractive index; (b) extinction coefficient as a function of wavelength, extracted from reflectance and absorbance spectra, respectively, by applying the Kramers-Kronig relationships; (c) The real and (d) imaginary parts of dielectric constant as a function of wavelength, extrapolated from the n and k indices; (e) The Tauc plots for this set of InSb thin film allow to identify the band gap energy. The inset of this figure presents the extracted ban gap energy depending on the T_d; and (f) The comparison between values of calculated $D_{average}$ (from XRD) and Bohr exciton diameter – $d_B = 2r_B$ for observable quantum confinement effect, as a function of T_d.

The optical properties for this set of films grown at various T_d are compiled in Figure 9. Prior to device fabrication, the refractive index – n, extinction coefficient – k, dielectric constant – ε_d, and band gap energy - E_g are among useful parameters in gaining insight into the electronic band gap structure that need characterizing. Figure 9a and b demonstrate the n and k spectral distributions over the

wavelength range, extracted from the FTIR measurement of reflectance and absorbance spectra (data not shown here), by applying the Kramers-Kronig relationships [54] embedded in the software in the FTIR equipment. The *n* and *k* indices reveal some oscillation appearances of extrema, which could be resulted from the interference between the two interfaces of air-film and film-substrate. The *n* index distribution varies with respect to incident wavelength (Figure 9a). Typically, the *n* indices of films deposited at low T_d are higher than those of films deposited at higher T_d, i. e., in everage, they are highest for RT film, and reach minima for 350 °C film, then lightly increase in 400 °C film. The significant correlation between the macroscopic parameter – density and refractive index – *n*, of thin film has been well established by employing light dispersion theory, which is based on Lorentz – Lorentz equation governed by Claussius – Mossotti relation [54–56]. According to the relation, the increase of *n* index might be attributed to the growth of the film density. This analysis is consistent with the reduction of film density resulted in more more porosity, and voids in films with isolated islands fashion at high T_d (Figure 4 and Figure 5).

The variation of *k* indices (in Figure 9b) are in contrast with observation for *n* indices, i. e., while *k* indices are highest for film with T_d = 350 °C, they have lower values for films at other T_d. It should be noted that the *k* values approach to zero value regime which can be attributed to the following concerns [57–59]: (i) the provided alloy InSb target from Neyco might still have a certain level of impurities (analyzed certificate delivered with the target, data not shown here); (ii) it is high possibility to form oxide layers on top of deposited films as films were exposed to the air after several characterizations (AFM, SEM, XRD, etc). For InSb, those oxide layers are usually transparent; and (iii) the crystallite sizes are experimentally estimated of over 100 nm (as evidenced in Figure 3b), which can be supposed as particles immersed in an absorbing host medium of InSb matrix. The real part - ε_r and imaginary part – ε_i of dielectric constant - $\varepsilon_d = \sqrt{\varepsilon_r^2 + \varepsilon_i^2}$ can be calculated from the *n* and *k* indices by applying the following relations [60]:

$$\varepsilon_r = n^2 - k^2 \qquad \text{Equation 6}$$

$$\varepsilon_i = 2nk \qquad \text{Equation 7}$$

Figure 9a and b illustrates the real and imaginary parts of dielectric constant as a function of the wavelength, using Equation 6 and Equation 7. The ε_r and ε_i values follow similar tendencies as *n* and *k* indices, respectively. The ε_r values are larger than those of values ε_i in almost the entire investigated wavelength range.

The band gap energies of the deposited films were estimated, based on the FTIR measurement and Kudelka - Munk model for observable optical parameters. The Kudelka - Munk model can be read as Equation 8 [61]. The relationship between energy of incident radiation – *hv* and E_g in Equation 9 is derived from Equation 8:

$$F(R) = (1-R)^2 / 2R \qquad \text{Equation 8}$$

$$[F(R)hv]^f = A(hv - E_g) \qquad \text{Equation 9}$$

where *F*(*R*) is known as absorption coefficient, *R* is the reflectivity, *A* is a coefficient depending on transition probability, and *f* is a power factor relating to optical absorption process. The semiconductors are often of two values for *f*, which can be 2 and 1/2 for materials with direct and indirect transition type semiconductor [62], respectively. Owing to the thin films deposited from direct transition type material – InSb, thus *f* is chosen *f* = 2. Graph of Equation 9 is known as Tauc plot, allowing to identify the E_g, by taking the intersection between the horizontal axis and the linear fit of the highest slope part. The Tauc plots for deposited InSb films at the low energy portion of the spectra are presented in Figure 9e.

Dependence of extrapolated E_g on T_d of deposited films is exhibited in inset of Figure 9e, which are all above the E_g = 0.17 eV of the bulk material [6]. The E_g values start with ~0.27 eV with T_d = RT and increase nearly two folds to ~0.50 eV with T_d = 300 °C, comparable to value 0.53 eV in film electrochemically fabricated [52]. The E_g then decreases with increasing T_d in the range T_d = 300 °C to 400 °C. Obviously, the T_d results in modification of the film crystallinity, grain size, and film composition. Depending on the employed T_d in the range from RT to 400 °C, the E_g can be tuned from the bulk value of 0.17 eV to 0.50 eV. In addition, the T_d might make an equivalent contribution in controlling the E_g as the film thickness ranging from 150 nm to 2000 nm, demonstrated in our previous study [63]. And it is therefore the E_g is a complex function of various variables that both T_d and film thickness induce. Proper combining these parameters could significantly encourage in achieving desirable InSb thin film for future development.

High values of E_g compared to that of the bulk form could be consistently assigned to the quantum confinement [64–66] and/or Burstein–Moss shift [67,68]. The quantum confinement relating to E_g can be written as:

$$E_g = E_g^o + \sqrt{\left(E_g^o\right)^2 + \frac{h^2 E_g^o}{2m^* r_B^2}} \qquad \text{Equation 10}$$

where E_g^o, h, $\frac{1}{m^*} = \frac{1}{m_e^*} + \frac{1}{m_h^*}$, and $r_B = \frac{2\varepsilon_d \varepsilon_o h}{m^* e^2} = \frac{d_B}{2}$ are the band gap energy of InSb with bulk form, Planck constant, reduced mass of the excitation, and Bohr exciton radius respectively. In this work, the effective mass of electron - m_e^* ($0.03m_o$, m_o – the free electron mass) and hole - m_h^* ($0.41m_o$) were taken from literature [69], the dielectric constant - ε_d were obtained from Figure 9a and b. The ε_d values were taken at the wavelength corresponding to the E_g. They are equal to 14.97, 10.08, 11.22, 16.37, 5.57, and 10.34 for T_d = RT, 200 °C, 250 °C, 300 °C, 350 °C, and 400 °C. Undoubtedly, because of the calculated d_B (Figure 9f) two times smaller than those of the D_{ave} estimated from XRD (Figure 3b), the system falls in the strong observable quantum confinement, in films deposited $T_d \leq 300$ °C. The estimated d_B for quantum confinement taking place is comparable with values of ~130 nm in GaAs nanowires [70], and larger in other nanowire systems, typically around 60 nm [64–66]. The quantum confinement (expressed in Equation 10) leads to an upgrade of $\Delta E_{quantum}$ ~0.18 eV from fundamental value of ~0.17 eV in the bulk InSb. The further E_g broadening of film (T_d = 300 °C) with $\Delta E_{B\text{-}M}$ = 0.50 eV – 0.17 eV – 0.18 eV = 0.15 eV, or films (T_d = 350 °C; $\Delta E_{B\text{-}M}$ = 0.50 eV, and 400 °C; $\Delta E_{B\text{-}M}$ = 0.01 eV, where the quantum confinement does not include because $d_B < D_{average}$), might be associated with band-filling effect of the so-called Burstein–Moss shift [67,68,71]. The Burstein–Moss shift is directly influenced by charge carrier concentration – n ($\Delta E_{B\text{-}M} \sim n^{2/3}$) reflected by the dislocation density (estimated in Figure 3b) for which the free electrons is introduced into conduction band resulting in widening of the optical E_g. In a nutshell, the optical E_g are strongly related to the density of localized states and sizes of crystallites (bulk, nanowire, thin film forms; order of arrangement – short (amorphous), long (crystallization with specific structure) range order, reflected by both quantum confinement and band-filling effects.

In short, the development of InSb films onto convential heated Si substrate under ultrahigh vacuum by PLD, at various deposition temperature provides additional comprehension of the augmentation of the InSb thin films, which opens new routes in characterizing for this type of material, and in fact, a blueprint in achieving exploration of the potential use of InSb thin films based material towards promising optoelectric devices.

IV. Conclusions

500 nm of nearly equi-atomic InSb thin films were well grown on conventional Si substrates, in a wide range of T_d, in vacuum, by means of PLD. The compositional, structural, morphological and optical properties were investigated. The prepared films demonstrate that T_d plays a key role during the film growth. Films developed above RT start showing preferential orientation of (h11) of ZB structure, and microstructural evolution from continuous patterns to island growth with increasing T_d. While the $D_{average}$, *LOF*, and $roughness_{rms}$ grow with T_d, the σ and ε reduce. Raman spectroscopy and XPS characterization reveal that all films are of two typical phonon vibration mode of TO and LO, with part of the films having oxidation. Varying the T_d allows to tune the optical E_g of nearly three folds compared to the bulk form (0.17 eV). The evolution of the optical E_g could be attributed to quantum confinement effect associated with Burstein–Moss shift, at which the crystallite sizes are smaller than the Bohr exciton diameters and the introduction of free electrons into the conduction band.

Author Contributions

Tuan NGUYEN VAN, Thin PHAM VAN: Conceptualization; Tuan NGUYEN VAN, Corinne CHAMPEAUX, Frédéric DUMAS-BOUCHIAT: Sample fabrication; Tuan NGUYEN VAN, Corinne CHAMPEAUX, Frédéric DUMAS-BOUCHIAT: Wrote original draft of the manuscript; Etienne LABORDE, Dat TRAN QUANG, Tung NGUYEN VU, Ca NGUYEN XUAN, Giang DO THI HUONG: Experimental characterization; Tuan NGUYEN VAN, Frédéric DUMAS-BOUCHIAT, Thin PHAM VAN: Data curation, validation; Tuan NGUYEN VAN, Thin PHAM VAN, Frédéric DUMAS-BOUCHIAT: Supervision; Tuan NGUYEN VAN, Thin PHAM VAN, Corinne CHAMPEAUX, Frédéric DUMAS-BOUCHIAT: Review & editing. All authors have read, participated in the discussion of the results, and agreed to the published version of the manuscript.

Acknowledgments

We have no financial support to thank in this work

References

[1] R. Chau, B. Doyle, S. Datta, J. Kavalieros, K. Zhang, Integrated nanoelectronics for the future, Nature Mater. 6 (2007) 810–812. https://doi.org/10.1038/nmat2014.

[2] I. Vurgaftman, J.R. Meyer, L.R. Ram-Mohan, Band parameters for III–V compound semiconductors and their alloys, Journal of Applied Physics. 89 (2001) 5815–5875. https://doi.org/10.1063/1.1368156.

[3] C. Kuenzer, S. Dech, eds., Thermal Infrared Remote Sensing, Springer Netherlands, Dordrecht, 2013. https://doi.org/10.1007/978-94-007-6639-6.

[4] A. Freundlich, A. Alemu, Multi quantum well multijunction solar cell for space applications, Physica Status Solidi (c). 2 (2005) 2978–2981. https://doi.org/10.1002/pssc.200460720.

[5] I. Kimukin, N. Biyikli, T. Kartaloglu, O. Aytur, E. Ozbay, High-speed InSb photodetectors on GaAs for mid-IR applications, IEEE Journal of Selected Topics in Quantum Electronics. 10 (2004) 766–770. https://doi.org/10.1109/JSTQE.2004.833891.

[6] K. Hnida, J. Mech, G.D. Sulka, Template-assisted electrodeposition of indium–antimony nanowires – Comparison of electrochemical methods, Applied Surface Science. 287 (2013) 252–256. https://doi.org/10.1016/j.apsusc.2013.09.135.

[7] D. Li, H. Li, H. Sun, L. Zhao, Characterization of ultrathin InSb nanocrystals film deposited on SiO2/Si substrate, Nanoscale Research Letters. 6 (2011) 601. https://doi.org/10.1186/1556-276X-6-601.

[8] T. Miyazaki, S. Adachi, Optical properties of InSb films deposited on sapphire substrates by rf sputtering, Journal of Applied Physics. 70 (1991) 1672–1677. https://doi.org/10.1063/1.349535.

[9] J.E. Oh, P.K. Bhattacharya, Y.C. Chen, S. Tsukamoto, Molecular-beam epitaxial growth of high-quality InSb on InP and GaAs substrates, Journal of Applied Physics. 66 (1989) 3618–3621. https://doi.org/10.1063/1.344069.

[10] V. Senthilkumar, M. Thamilselvan, K. PremNazeer, Sa.K. Narayandass, D. Mangalaraj, B. Karunagaran, K. Kim, J. Yi, Characterization of p-type In–Sb thin films prepared by vacuum evaporation, Vacuum. 79 (2005) 163–170. https://doi.org/10.1016/j.vacuum.2005.03.004.

[11] L.H.-T. Li Deng-Yue, L.H.-T. Li Deng-Yue, Effects of rapid thermal annealing on the morphology and optical properity of ultrathin InSb film deposited on SiO2/Si substrate, Chin. Phys. B. 22 (2013) 27802–027802. https://doi.org/10.1088/1674-1056/22/2/027802.

[12] S.D. Wu, L.W. Guo, Z.H. Li, X.Z. Shang, W.X. Wang, Q. Huang, J.M. Zhou, Effect of the low-temperature buffer thickness on quality of InSb grown on GaAs substrate by molecular beam epitaxy, Journal of Crystal Growth. 277 (2005) 21–25. https://doi.org/10.1016/j.jcrysgro.2004.12.141.

[13] M.C. Debnath, T. Zhang, C. Roberts, L.F. Cohen, R.A. Stradling, High-mobility InSb thin films on GaAs (001) substrate grown by the two-step growth process, Journal of Crystal Growth. 267 (2004) 17–21. https://doi.org/10.1016/j.jcrysgro.2004.03.033.

[14] R. Venkataraghavan, K.M. Satyalakshmi, K.S.R.K. Rao, A.K. Sreedhar, M.S. Hegde, H.L. Bhat, Pulsed laser deposition of indium antimonide, Bull. Mater. Sci. 19 (1996) 123–129. https://doi.org/10.1007/BF02744794.

[15] E. Robert, Pulsed Laser Deposition of Thin Films: Applications-Led Growth of Functional Materials, John Wiley & Sons, Hoboken, New Jersey, 2006. https://onlinelibrary.wiley.com/doi/book/10.1002/0470052120.

[16] D.Y. Wang, P. Yun, Y. Wang, H.L.W. Chan, C.L. Choy, Influence of oxygen partial pressure on the structural and dielectric properties of Ba(Zr0.3Ti0.7)O3 thin films grown on (LaAlO3)0.3(Sr2AlTaO6)0.35 (001) using pulsed laser deposition, Thin Solid Films. 517 (2009) 2092–2098. https://doi.org/10.1016/j.tsf.2008.10.029.

[17] S.-M. Park, T. Ikegami, K. Ebihara, Effects of substrate temperature on the properties of Ga-doped ZnO by pulsed laser deposition, Thin Solid Films. 513 (2006) 90–94. https://doi.org/10.1016/j.tsf.2006.01.051.

[18] X. Song, D. Hong, Y. Wang, H. Liu, L. Liu, Y. Li, The Effect of Laser Energy and Target–Substrate Distance on the Quality of CeO2 Seed Layer Deposited by PLD, J Supercond Nov Magn. 24 (2011) 1659–1663. https://doi.org/10.1007/s10948-010-1080-6.

[19] E. van de Riet, C.J.C.M. Nillesen, J. Dieleman, Reduction of droplet emission and target roughening in laser ablation and deposition of metals, Journal of Applied Physics. 74 (1993) 2008–2012. https://doi.org/10.1063/1.354763.

[20] T. Nguyen Van, I. de Moraes, N.M. Dempsey, C. Champeaux, F. Dumas-Bouchiat, Textured Nd-Fe-B hard magnetic thin films prepared by pulsed laser deposition with single alloy targets, J. Magn. Magn. Mater. 520 (2021) 167584. https://doi.org/10.1016/j.jmmm.2020.167584.

[21] A. Ojeda-G-P, C.W. Schneider, M. Döbeli, T. Lippert, A. Wokaun, Plasma plume dynamics, rebound, and recoating of the ablation target in pulsed laser deposition, Journal of Applied Physics. 121 (2017) 135306. https://doi.org/10.1063/1.4979780.

[22] Q. Zhao, F. Wang, K. Wang, G. Xie, W. Cui, J. Li, Effect of Sputtering Temperature on Fluorocarbon Films: Surface Nanostructure and Fluorine/Carbon Ratio, Nanomaterials. 9 (2019) 848. https://doi.org/10.3390/nano9060848.

[23] Y. Suzuki, H. Fu, Y. Abe, M. Kawamura, Effects of substrate temperature on structure and mechanical properties of sputter deposited fluorocarbon thin films, Vacuum. 87 (2013) 218–221. https://doi.org/10.1016/j.vacuum.2012.05.029.

[24] R. Alvarez, J.M. Garcia-Martin, M.C. Lopez-Santos, V. Rico, F.J. Ferrer, J. Cotrino, A.R. Gonzalez-Elipe, A. Palmero, On the Deposition Rates of Magnetron Sputtered Thin Films at Oblique Angles, Plasma Processes and Polymers. 11 (2014) 571–576. https://doi.org/10.1002/ppap.201300201.

[25] K.F. Hulme, J.B. Mullin, Indium antimonide—A review of its preparation, properties and device applications, Solid-State Electronics. 5 (1962) 211-IN10. https://doi.org/10.1016/0038-1101(62)90104-1.

[26] H. Landolt, R. Börnstein, K.H. Hellwege, D. Bimberg, M. Schulz, H. Weiss, O. Madelung, Landolt-Börnstein: Numerical data and functional relationships in science and technology. Group 3, Crystal and solid state physics. Vol. 17, Semiconductors, Springer, Berlin, 1982.

[27] O. Madelung, Semiconductors: data handbook, Springer, Berlin; New York, 2004.

[28] R. Delhez, Th.H. de Keijser, E.J. Mittemeijer, Determination of crystallite size and lattice distortions through X-ray diffraction line profile analysis, Z. Anal. Chem. 312 (1982) 1–16. https://doi.org/10.1007/BF00482725.

[29] H.P. Klug, L.E. Alexander, X-Ray Diffraction Procedures: For Polycrystalline and Amorphous Materials, 2nd Edition, New York, 1974.

[30] B.D. Cullity, Elements of x-ray diffraction, Addison-Wesley Publishing Company, Inc., Reading, MA, 1978.

[31] G.K. Williamson, W.H. Hall, X-ray line broadening from filed aluminium and wolfram, Acta Metallurgica. 1 (1953) 22–31. https://doi.org/10.1016/0001-6160(53)90006-6.

[32] G.K. Williamson, R.E. Smallman, III. Dislocation densities in some annealed and cold-worked metals from measurements on the X-ray debye-scherrer spectrum, The Philosophical Magazine: A Journal of Theoretical Experimental and Applied Physics. 1 (1956) 34–46. https://doi.org/10.1080/14786435608238074.

[33] C.G. Dunn, E.F. Kogh, Comparison of dislocation densities of primary and secondary recrystallization grains of Si-Fe, Acta Metallurgica. 5 (1957) 548–554. https://doi.org/10.1016/0001-6160(57)90122-0.

[34] S.R. Lee, A.M. West, A.A. Allerman, K.E. Waldrip, D.M. Follstaedt, P.P. Provencio, D.D. Koleske, C.R. Abernathy, Effect of threading dislocations on the Bragg peakwidths of GaN, AlGaN, and AlN heterolayers, Appl. Phys. Lett. 86 (2005) 241904. https://doi.org/10.1063/1.1947367.

[35] J.E. Ayers, The measurement of threading dislocation densities in semiconductor crystals by X-ray diffraction, Journal of Crystal Growth. 135 (1994) 71–77. https://doi.org/10.1016/0022-0248(94)90727-7.

[36] R. Guinebretière, X-Ray Diffraction by Polycrystalline Materials, London ; Newport Beach, CA, 2007.

[37] V.S. Kopp, V.M. Kaganer, M.V. Baidakova, W.V. Lundin, A.E. Nikolaev, E.V. Verkhovtceva, M.A. Yagovkina, N. Cherkashin, X-ray determination of threading dislocation densities in GaN/Al2O3(0001) films grown by metalorganic vapor phase epitaxy, Journal of Applied Physics. 115 (2014) 073507. https://doi.org/10.1063/1.4865502.

[38] J. Yu, Z. Hao, L. Li, L. Wang, Y. Luo, J. Wang, C. Sun, Y. Han, B. Xiong, H. Li, Influence of dislocation density on internal quantum efficiency of GaN-based semiconductors, AIP Advances. 7 (2017) 035321. https://doi.org/10.1063/1.4979504.

[39] J. Samuels, S.G. Roberts, P.B. Hirsch, The brittle–ductile transition in silicon. I. Experiments, Proceedings of the Royal Society of London. A. Mathematical and Physical Sciences. 421 (1989) 1–23. https://doi.org/10.1098/rspa.1989.0001.

[40] J.M. Wheeler, L. Thilly, Y. Zou, A. Morel, R. Raghavan, J. Michler, The effect of dislocation nature on the size effect in Indium Antimonide above and below the brittle-ductile transition, MRS Advances. 5 (2020) 1811–1818. https://doi.org/10.1557/adv.2019.369.

[41] F.K. Lotgering, Topotactical reactions with ferrimagnetic oxides having hexagonal crystal structures—I, Journal of Inorganic and Nuclear Chemistry. 9 (1959) 113–123. https://doi.org/10.1016/0022-1902(59)80070-1.

[42] L. Ratke, P.W. Voorhees, Growth and Coarsening: Ostwald Ripening in Material Processing, Springer-Verlag, Berlin Heidelberg, 2002. https://doi.org/10.1007/978-3-662-04884-9.

[43] P.D. Szkutnik, A. Karmous, F. Bassani, A. Ronda, I. Berbezier, K. Gacem, A.E. Hdiy, M. Troyon, Ge nanocrystals formation on SiO2 by dewetting: application to memory, Eur. Phys. J. Appl. Phys. 41 (2008) 103–106. https://doi.org/10.1051/epjap:2008006.

[44] A. Pinczuk, E. Burstein, Raman Scattering from InSb Surfaces at Photon Energies Near the E1 Energy Gap, Phys. Rev. Lett. 21 (1968) 1073–1075. https://doi.org/10.1103/PhysRevLett.21.1073.

[45] W. Kiefer, W. Richter, M. Cardona, Second-order Raman scattering in InSb, Phys. Rev. B. 12 (1975) 2346–2354. https://doi.org/10.1103/PhysRevB.12.2346.

[46] A.T. Vogel, J. de Boor, M. Becker, J.V. Wittemann, S.L. Mensah, P. Werner, V. Schmidt, Ag-assisted CBE growth of ordered InSb nanowire arrays, Nanotechnology. 22 (2010) 015605. https://doi.org/10.1088/0957-4484/22/1/015605.

[47] S.V. Demishev, Yu.V. Kosichkin, A.G. Lyapin, N.N. Mel'Nik, D.V. Nekhaev, N.E. Sluchanko, O.A. Turok, Raman scattering in amorphous gallium antimonide, Soviet Journal of Experimental and Theoretical Physics. 77 (1993) 329–336. http://adsabs.harvard.edu/abs/1993JETP...77..329D (accessed March 25, 2021).

[48] Z. Algarni, A. Singh, U. Philipose, Synthesis of Amorphous InSb Nanowires and a Study of the Effects of Laser Radiation and Thermal Annealing on Nanowire Crystallinity, Nanomaterials. 8 (2018) 607. https://doi.org/10.3390/nano8080607.

[49] J.S. Lannin, Low frequency Raman scattering in amorphous materials: a-Ge, a-InSb, and a-Ge0.5Sn0.5, Solid State Communications. 11 (1972) 1523–1527. https://doi.org/10.1016/0038-1098(72)90513-3.

[50] S.R. Das, C. Akatay, A. Mohammad, M.R. Khan, K. Maeda, R.S. Deacon, K. Ishibashi, Y.P. Chen, T.D. Sands, M.A. Alam, D.B. Janes, Electrodeposition of InSb branched nanowires: Controlled growth with structurally tailored properties, Journal of Applied Physics. 116 (2014) 083506. https://doi.org/10.1063/1.4893704.

[51] X. Tang, R.G. van Welzenis, F.M. van Setten, A.J. Bosch, Oxidation of the InSb surface at room temperature, Semicond. Sci. Technol. 1 (1986) 355–365. https://doi.org/10.1088/0268-1242/1/6/004.

[52] K. E. Hnida, S. Bäßler, J. Mech, K. Szaciłowski, R. P. Socha, M. Gajewska, K. Nielsch, M. Przybylski, G. D. Sulka, Electrochemically deposited nanocrystalline InSb thin films and their electrical properties, Journal of Materials Chemistry C. 4 (2016) 1345–1350. https://doi.org/10.1039/C5TC03656A.

[53] W.K. Liu, W.T. Yuen, R.A. Stradling, Preparation of InSb substrates for molecular beam epitaxy, Journal of Vacuum Science & Technology B: Microelectronics and Nanometer Structures

Processing, Measurement, and Phenomena. 13 (1995) 1539–1545. https://doi.org/10.1116/1.588184.

[54] V. Lucarini, J.J. Saarinen, K.-E. Peiponen, E.M. Vartiainen, Kramers-Kronig relations in optical materials research, 1st ed., Springer-Verlag Berlin Heidelberg, 2005. https://doi.org/10.1007/b138913.

[55] D.E. Aspnes, Optical properties of thin films, Thin Solid Films. 89 (1982) 249–262. https://doi.org/10.1016/0040-6090(82)90590-9.

[56] D.E. Aspnes, Local-field effects and effective-medium theory: A microscopic perspective, American Journal of Physics. 50 (1982) 704–709. https://doi.org/10.1119/1.12734.

[57] M.I. Mishchenko, G. Videen, P. Yang, Extinction by a homogeneous spherical particle in an absorbing medium, Opt. Lett., OL. 42 (2017) 4873–4876. https://doi.org/10.1364/OL.42.004873.

[58] M.I. Mishchenko, J.M. Dlugach, Scattering and extinction by spherical particles immersed in an absorbing host medium, Journal of Quantitative Spectroscopy and Radiative Transfer. 211 (2018) 179–187. https://doi.org/10.1016/j.jqsrt.2018.03.001.

[59] N. Kikuchi, H. Hosono, H. Kawazoe, O. Tanegashima, I. Ota, Y. Kimura, Transparent conducting oxide, InSbO4 with random rutile structure, Vacuum. 65 (2002) 81–84. https://doi.org/10.1016/S0042-207X(01)00410-9.

[60] G.A.N. Connell, R.J. Temkin, W. Paul, Amorphous germanium III. Optical properties, Advances in Physics. 22 (1973) 643–665. https://doi.org/10.1080/00018737300101359.

[61] G. Kortüm, Reflectance Spectroscopy: Principles, Methods, Applications, Springer-Verlag, Berlin Heidelberg, 1969. https://doi.org/10.1007/978-3-642-88071-1.

[62] J. Tauc, ed., Amorphous and Liquid Semiconductors, Springer US, 1974. https://doi.org/10.1007/978-1-4615-8705-7.

[63] Van T.P., Thi P.D.D., Vu T.N., Quang D.T., Thanh N.N., Van T.N., Ảnh hưởng của độ dày lên tính chất màng mỏng InSb chế tạo bằng phương pháp lắng đọng laser xung trên đế Silic, Journal of Military Science and Technology. (2022) 109–118. https://doi.org/10.54939/1859-1043.j.mst.84.2022.109-118.

[64] I.H. Campbell, P.M. Fauchet, The effects of microcrystal size and shape on the one phonon Raman spectra of crystalline semiconductors, Solid State Communications. 58 (1986) 739–741. https://doi.org/10.1016/0038-1098(86)90513-2.

[65] H. Richter, Z.P. Wang, L. Ley, The one phonon Raman spectrum in microcrystalline silicon, Solid State Communications. 39 (1981) 625–629. https://doi.org/10.1016/0038-1098(81)90337-9.

[66] R. Winkler, Excitons and fundamental absorption in quantum wells, Phys. Rev. B. 51 (1995) 14395–14409. https://doi.org/10.1103/PhysRevB.51.14395.

[67] K.G. Saw, N.M. Aznan, F.K. Yam, S.S. Ng, S.Y. Pung, New Insights on the Burstein-Moss Shift and Band Gap Narrowing in Indium-Doped Zinc Oxide Thin Films, PLOS ONE. 10 (2015) e0141180. https://doi.org/10.1371/journal.pone.0141180.

[68] P.K. Chakraborty, B.N. Mondal, G. Sardar, Simple theoretical analyses of the Burstein–Moss shift (BMS) revisited for n-GaAs semiconductor with and without band-tailing conditions, Indian J Phys. 95 (2021) 443–448. https://doi.org/10.1007/s12648-020-01730-6.

[69] N. Bouarissa, H. Aourag, Effective masses of electrons and heavy holes in InAs, InSb, GaSb, GaAs and some of their ternary compounds, Infrared Physics & Technology. 40 (1999) 343–349. https://doi.org/10.1016/S1350-4495(99)00020-1.

[70] F. Kargar, B. Debnath, J.-P. Kakko, A. Säynätjoki, H. Lipsanen, D.L. Nika, R.K. Lake, A.A. Balandin, Direct observation of confined acoustic phonon polarization branches in free-standing semiconductor nanowires, Nat Commun. 7 (2016) 13400. https://doi.org/10.1038/ncomms13400.

[71] E. Burstein, Anomalous Optical Absorption Limit in InSb, Phys. Rev. 93 (1954) 632–633. https://doi.org/10.1103/PhysRev.93.632.

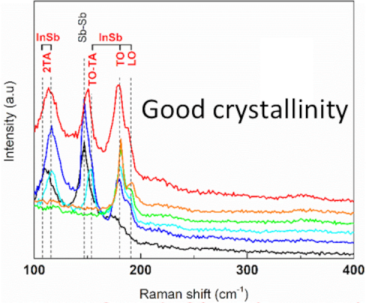

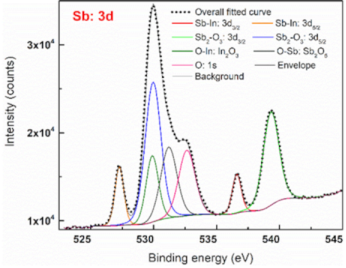

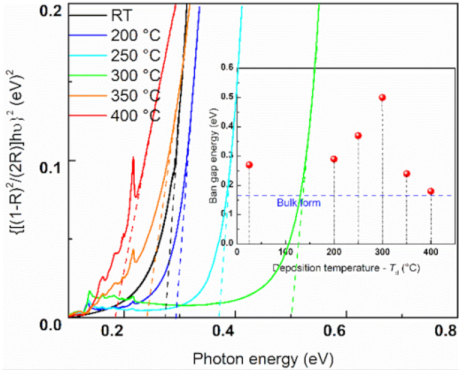

A set of InSb films deposited by PLD, at UHV, and various deposition temperatures, onto heated Si